

# Vortex development behind a finite porous obstruction in a channel

Lijun Zong<sup>†</sup> and Heidi Nepf

48-216, Department of Civil and Environmental Engineering, Massachusetts Institute of Technology,  
Cambridge, MA 02139, USA

(Received 25 May 2011; revised 20 October 2011; accepted 27 October 2011;  
first published online 6 December 2011)

This experimental study describes the turbulent wake behind a two-dimensional porous obstruction, consisting of a circular array of cylinders. The cylinders extend from the channel bed through the water surface, mimicking a patch of emergent vegetation. Three patch diameters ( $D$ ) and seven solid volume fractions ( $\Phi$ ) are tested. Because flow can pass through the patch, directly downstream there is a region of steady, non-zero, streamwise velocity,  $U_1$ , called the steady wake. For the patch diameters and solid volume fractions considered here,  $U_1$  is a function of  $\Phi$  only. The length of the steady wake ( $L_1$ ) increases as  $\Phi$  decreases and can be predicted from the growth of a plane shear layer. The formation of the von-Kármán vortex street is delayed until the end of the steady wake. There are two regions of elevated transverse velocity fluctuation ( $v_{rms}$ ): directly behind the patch, associated with the wake turbulence of individual cylinders; and at the distance  $L_1$  from the patch, associated with the formation of large-scale wake oscillation. Velocity along the centreline of the wake starts to increase only after the patch-scale vortex street is formed, and it approaches the free-stream velocity over a distance  $L_2$ . The dimensionless length of the entire wake,  $(L_1 + L_2)/D$ , increases with patch porosity.

**Key words:** shear layers, vortex streets, wakes

---

## 1. Introduction

Aquatic vegetation is ecologically and structurally important in natural channels. It provides habitat for animals, and it improves water quality and clarity by taking up nutrients and by trapping heavy metals and suspended particles (Gacia & Duarte 2001; Brookshire & Dwire 2003; Schultz *et al.* 2003; Windham, Weis & Weis 2003; Moore 2004; Cotton *et al.* 2006; Widdows, Pope & Brinsley 2008). Further, by altering the mean and turbulent flow field, vegetation can change the distribution of deposition and erosion, which ultimately controls the channel morphology (Fonseca *et al.* 1983; Bouma *et al.* 2007; Rominger, Lightbody & Nepf 2010).

Circular cylinders are often used to model rigid emergent vegetation, such as reeds, because they provide a good approximation of the stems. Cylinders piercing the water surface are placed in staggered, square-grid or random arrangements. Cylinder arrays that cover the entire flume width have been used to estimate the bulk drag coefficient,

<sup>†</sup> Email address for correspondence: [lz248@mit.edu](mailto:lz248@mit.edu)

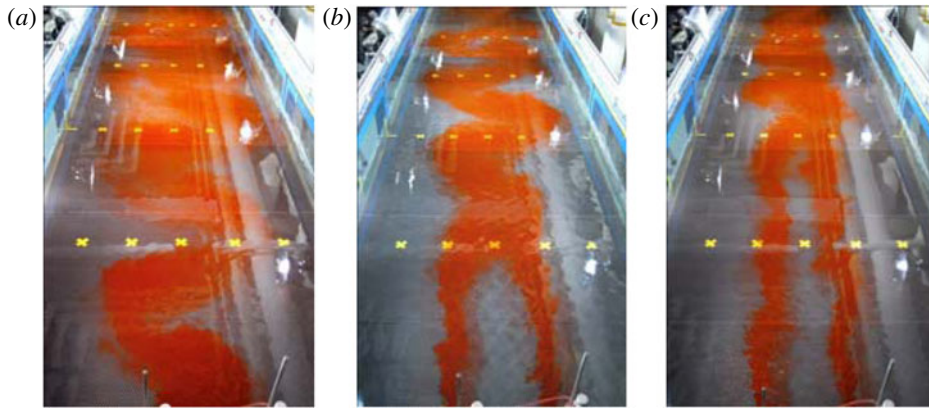


FIGURE 1. The two-dimensional wakes behind three porous obstructions of diameter  $D = 22$  cm, with different solid volume fraction,  $\Phi = 1, 0.10, 0.03$ , ( $a-c$ ), respectively. The flume is 1.2 m wide. The obstruction is placed in the middle of the flume and is located just below the bottom of each picture. The struts holding the dye injection system are visible. Flow is from bottom to top of the image. The rows of crosses mark 1 m intervals from the upstream end of the patch. The lateral distance between markers in the same row is 20 cm.

and to study the diffusion and dispersion within the array (e.g. Nepf 1999; Stone & Shen 2002; Sharpe & James 2006; Tanino & Nepf 2008). Through numerical modelling, Lopez & Garcia (1998) show that the suspended sediment transport is reduced in vegetated waterways, due to reduced bed shear stress. Sharpe & James (2006), White & Nepf (2007, 2008) and Zong & Nepf (2011) studied the lateral exchange between a free stream and an adjacent parallel region of model vegetation. However, only a few projects have considered finite patches of model vegetation, with length and width scales smaller than the channel width. Yet, this configuration is common in the field (e.g. Sand-Jensen & Pedersen 2008).

A few previous studies have considered flow past finite porous obstructions. Ball, Stansby & Alliston (1996), Takemura & Tanaka (2007) and Nicolle & Eames (2011) each used a group of cylinders to model a finite porous body and investigated the flow through and around the group. Castro (1971), Chen & Jirka (1995) and Huang & Keffer (1996) investigated the wake structure behind a porous plate. Despite using different shapes and sizes for the porous body, these studies all show that the wake behind a porous obstruction is different from that behind a solid body. In particular, as the porosity of the obstruction increases, the von-Kármán vortex street originates further downstream in the wake. The region from the porous body to the formation point of the vortex street is called the steady wake region. In Castro's (1971) experiments, the vortex street does not form at all for porosity greater than 0.2. The injection of flow from the trailing edge of a solid body (called base bleed) produces a similar wake structure, i.e. it creates a steady wake region directly behind the obstruction (Wood 1967). Wood (1967) observed that as the bleed flow increased, the vortex formation moved further downstream.

In this study, we observe the wake structure behind a two-dimensional, circular porous obstruction (representing a patch of model emergent vegetation). For example, the wake structure observed behind the circular patches with solid volume fractions of 1 (solid body), 0.10 and 0.03 are shown in figure 1( $a-c$ ), respectively. Dye is injected at the two sides of the patch or solid body. Behind the solid body (figure 1 $a$ ), the

dye is swept into the familiar von-Kármán vortex street immediately downstream of the obstruction. In contrast, for the porous cases (*b*) and (*c*), there is a region directly behind the porous body, the steady wake region, in which the dye moves along straight lines with no lateral motion. The single vortex street does not form until some distance downstream. As the solid volume fraction ( $\Phi$ ) decreases from 0.10 (figure 1*b*) to 0.03 (figure 1*c*), i.e. porosity increases, the initiation of the vortex street occurs further downstream, and the lateral extent of the vortex street becomes smaller, suggesting that the strength of the vortices in the street has decreased.

The numerical study by Nicolle & Eames (2011) also considered patches of circular cylinders and suggests three distinct flow regimes. For low solid volume fractions ( $\Phi < 0.05$ ), the individual cylinders are sufficiently far apart that the flow interactions within the array are weak. Vortices form behind individual cylinders, but no patch-scale vortex street is formed. At intermediate solid volume fractions ( $0.05 < \Phi < 0.15$ ), a steady wake forms directly behind the cylinder array, and a vortex street forms at some distance downstream from the patch (similar to figure 1*b,c*). For high solid volume fractions ( $\Phi > 0.15$ ), the cylinder array generates a wake that is similar to a solid body (figure 1*a*). Nicolle & Eames (2011) considered a single patch diameter and varied the number of cylinders within the patch. Here we will vary both the patch size as well as the cylinder density within the patch.

While previous studies have revealed the presence of a steady wake region behind a porous obstruction, they have not provided a model for predicting the length scale of the steady wake ( $L_1$ ), or considered the role of the steady wake velocity scale ( $U_1$ ). In this study, we provide a more detailed description of the wake structure using velocity measurements and flow visualization, and use this detail to support a theoretical model to predict both  $L_1$  and  $U_1$ .

## 2. Experiment methods

Experiments were conducted in a 16 m long re-circulating flume with a test section that has a width ( $B$ ) of 1.2 m and a length of 13 m. The bed of the flume is horizontal. Circular porous obstructions were constructed with circular cylinders of diameter  $d = 0.6$  cm that extended from the bed through the water surface and were set in a staggered arrangement (figure 2*a*). The patches were placed at the centre of the flume, beginning 3 m from the start of the test section. Individual cylinders were held in place by perforated PVC baseboards that extended over the entire flume bed. Three patch sizes were tested, with diameters of  $D = 12, 22$  and 42 cm. The density of the cylinders within the patch is described by the following parameters: the number of cylinders per unit bed area,  $n$  ( $\text{cm}^{-2}$ ), the frontal area per unit volume,  $a = nd$  ( $\text{cm}^{-1}$ ), the average solid volume fraction,  $\Phi = n\pi d^2/4 \approx ad$ , and the porosity,  $\beta = 1 - \Phi$ . This study considered patches with  $\Phi = 0.03$  to 0.36 and also  $\Phi = 1$ , i.e. a solid obstruction (see table 1). A constant upstream velocity was used,  $U_\infty = 9.8 \pm 0.5$   $\text{cm s}^{-1}$ . A weir at the downstream end of the test section controlled the water depth,  $h = 13.3 \pm 0.2$  cm. The  $x$ -axis points in the direction of flow with  $x = 0$  at the patch leading edge. The  $y$ -axis is in the transverse direction, with  $y = 0$  at the patch centreline (figure 2*b*).

From measured bed shear velocity,  $u_*$ , and depth-average velocity,  $U$ , we define a quadratic-law bed friction coefficient,  $C_f = u_*^2/U^2$ . The bottom friction coefficient  $C_f = 0.006$  was measured in a previous study over the same baseboards (White & Nepf 2007, 2008). In shallow flow, the bed friction may suppress the vortex street behind a solid circular obstruction, if the stability parameter  $S = C_f D/h$  is

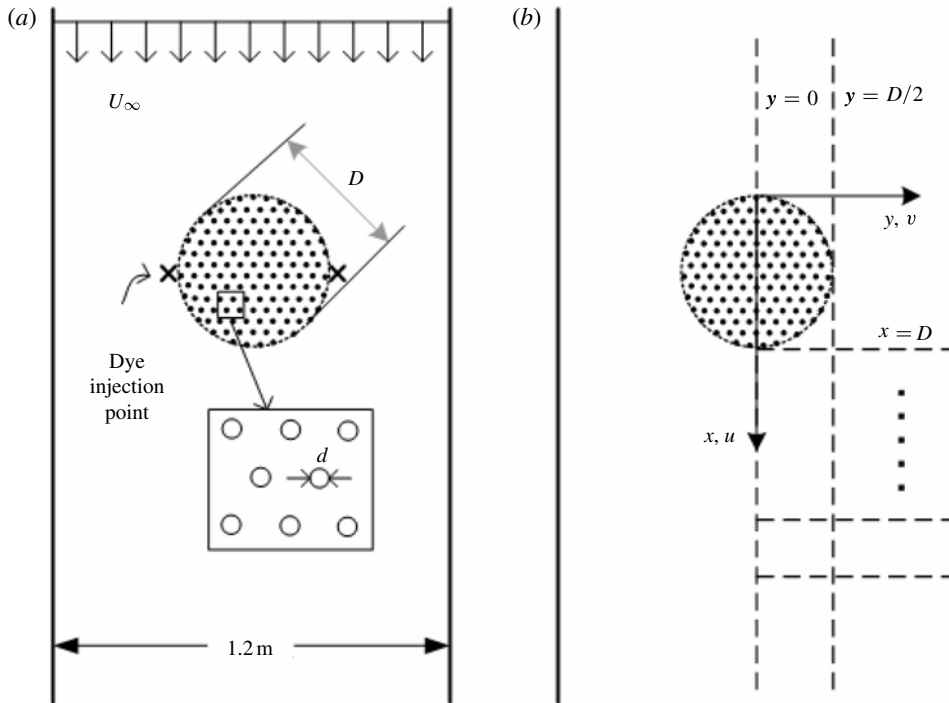


FIGURE 2. Top view of experiment setup. (a) Patch configuration and dye injection points; (b) longitudinal and lateral transects (dashed lines) of velocity measurements.  $x = 0$  is at the upstream edge of the patch,  $y = 0$  is at the centreline of the patch.

greater than a critical value,  $S_c = 0.2$  (Chen & Jirka 1995). Chen & Jirka (1995) also considered a porous plate ( $\Phi = 0.5$ ), for which they found  $S_c = 0.09$ . In our experiments,  $S = 0.019, 0.010$  and  $0.005$  for patch diameters  $D = 42, 22$  and  $12$  cm, respectively, which are all well below the critical value. Therefore, in our cases the bed friction is not large enough to suppress the vortex shedding process.

The influence of the channel blockage, i.e. the ratio of the obstruction diameter ( $D$ ) to channel width ( $B$ ), should be considered. For our patches,  $D/B$  is  $0.10, 0.18$  and  $0.35$  for  $D = 12, 22$  and  $42$  cm, respectively. Some previous studies have considered how channel blockage impacts the shedding frequency ( $f_D$ ), or specifically the Strouhal number ( $St_D$ ). The critical Reynolds number ( $Re_c$ ), at which an unbounded steady flow past a circular cylinder becomes unstable, is  $Re_c = 47$  and its corresponding Strouhal number is  $St_D \approx 0.12$  (Norberg 1994). Chen, Pritchard & Tavener (1995) and Coutanceau & Bouard (1977) reported that both  $Re_c$  and  $St_D$  increase with increasing channel blockage. For a blockage  $0.64$ , Sahin & Owens (2004) found  $Re_c$  and  $St_D$  were  $285$  and  $0.44$ , respectively. For  $Re_D$  between  $100$  and  $300$ , Turki, Abbassi & Nasrallah (2003) showed  $St_D$  increases with increasing channel blockage. In this study,  $Re_D$  is  $O(10^4)$ , which is within the regime of turbulent wakes. Therefore, channel blockage might have some influence on the vortex shedding frequency in our study. In addition, at the highest channel blockage ( $D/B = 0.35$ ), the flow forced through the patch might be increased, relative to an unbounded case. These effects are explored in the discussion of results.

$D$ (cm)	42	42	22	22	22	22	22	22	12	12
$a$ ( $\text{cm}^{-1}$ )	Solid	0.20	0.06	Solid	0.77	0.29	0.20	0.09	0.06	0.20
$\Phi$	1	0.10	0.03	1	0.36	0.14	0.10	0.05	0.03	0.10
$U_\infty \pm 0.1 \text{ cm s}^{-1}$	9.8	9.7	9.6	9.8	9.7	9.7	9.9	9.6	9.8	9.8
$U_1 \pm 0.1 \text{ cm s}^{-1}$	0	0.5	5.0	0	0	0.3	0.3	3.8	5.8	0.7
$U_2 \pm 0.3 \text{ cm s}^{-1}$	15.1	15.0	13.0	13.1	13.0	12.8	13.0	12.1	11.6	11.0
$U_1/U_2$	0	0.03	0.38	0	0	0.02	0.02	0.31	0.5	0.06
$v_{rms,max} \pm 0.1 \text{ cm s}^{-1}$	6.1	4.7	1.3	7.0	6.0	3.7	3.3	1.6	1.0	2.2
$L_1$ (cm)	0	110	260	0	0	70	63	130	178	55
		(10)	(10)			(5)	(5)	(10)	(10)	(5)
$L_2$ (cm)	140	170	400	65	90	90	85	175	200	95
	(10)	(20)	(30)	(5)	(5)	(15)	(15)	(30)	(20)	(15)
$L_{1,dve}$ (cm) from flow visual.	a	90	310	0	0	45	65	120	160	45
		(10)	(20)			(5)	(5)	(10)	(10)	(5)
$L_1$ (cm) from (4.3)	0	120	245	0	0	60	60	110	170	35
		(30)	(65)			(15)	(15)	(30)	(45)	(10)
Position of $v_{rms,max}$ (cm), measured from $x = D$	53	168	408	18	23	98	98	208	328	83
	(5)	(5)	(20)	(5)	(5)	(5)	(10)	(10)	(20)	(5)
$St_D = f_D D / U_2$ ( $f_D$ from spectrum)	0.20	0.20	0.24	0.16	0.17	0.17	0.16	0.17	0.18	0.16
$St_D$ ( $f_D$ from flow visual.)	a	0.20	—	0.17	0.17	0.17	0.17	0.20	—	0.18

TABLE 1. Summary of parameters. Numbers in brackets are the uncertainties of the parameters. <sup>a</sup> No flow visualization – vortex street not distinct in flow visualization.

To characterize the flow field, velocity measurements were taken using a Nortek Vectrino, with a sampling volume 6 mm across and 3 mm high. This probe measures all three velocity components, but, since we consider the flow to be two-dimensional, we only present the horizontal components. The vertical component was only analysed to verify the orientation of the probe. The probe was mounted on a platform that could be moved along and across the flume. The probe was manually positioned, with a positioning accuracy of  $\pm 0.5$  cm in the  $y$ -direction and  $\pm 1$  cm in the  $x$ -direction. Longitudinal transects were made through the centreline of the circular patch ( $y = 0$ ) and along the edge of the patch ( $y = D/2$ ), as shown in figure 2(b). The longitudinal profiles started 1 m upstream of the patch ( $x = -1$  m) and extended 5–9 m downstream of the patch, depending on the patch size. Because of the difficulty in placing the Vectrino probe head within the densest patches, no velocity measurements were made within the patch. Lateral profiles were taken at several positions behind the patch. Owing to the symmetry about the centreline ( $y = 0$ ), the lateral profiles were only taken across half of the flume width (from the centreline to a sidewall, figure 2b). In order to compare the flow fields of a porous body and a solid body, waterproof contact paper was wrapped around the circumference of the porous body, creating a solid body of the same diameter. Similar velocity transects were made for the solid obstruction.

At each measurement point the instantaneous longitudinal,  $u(t)$ , and lateral,  $v(t)$ , components of the velocity were recorded at mid-depth for 240 s at a sample rate of 25 Hz. Based on previous studies with emergent obstructions (e.g. White & Nepf 2007), the velocity measured at mid-depth is a good approximation of the depth-averaged velocity, which may be used to represent the approximately two-dimensional behaviour of the flow. Three-dimensional effects associated with the bottom boundary layer are of second order and will not be considered here. Each record was decomposed into its time-average,  $(\bar{u}, \bar{v})$ , and fluctuating components,  $(u'(t), v'(t))$ . The overbar denotes the time-average. The intensity of turbulent fluctuations was estimated as the root-mean-square of the fluctuating velocity,  $u_{rms} = \sqrt{\overline{(u')^2}}$  and  $v_{rms} = \sqrt{\overline{(v')^2}}$ . The mean velocity had an uncertainty of  $\pm 0.1$  cm s<sup>-1</sup>. Measurements made in still water determined the instrument noise,  $u_{rms,noise} = 0.3$  cm s<sup>-1</sup>, which sets the lower limit at which turbulence intensity can be resolved. Instantaneous records of cross-stream velocity,  $v$ , were used to evaluate the velocity spectrum,  $S_{vv}$ , by the Welch's method, as described in MATLAB toolbox.

Flow visualization was used to examine the wake structure. Red dye was injected at the outermost edges of the circular patch (figure 2a) with a constant flow rate which matched the ambient. The duration of injection was 2 min. The camera was positioned about 1 m above the flume in order to capture a 6 m region directly behind the patch. Pictures were taken at 2 s intervals for 1 min duration and were post-processed using Photoshop software in order to enhance the colour of the dye. Tape was used to mark positions at 50 cm intervals in the  $x$ -direction and 20 cm intervals in the  $y$ -direction. Grids determined by these markers were superposed onto the pictures.

### 3. Results

#### 3.1. Mean and turbulent velocity profiles

We consider the transverse velocity to indicate the beginning of flow diversion around the patch (solid circles and right-hand axis in figures 3b,c and 4b,c). However, because of the centreline symmetry, the mean transverse velocity is zero at  $y = 0$ . So, we show the transverse velocity measured at the outermost edge of the patch, along a transect



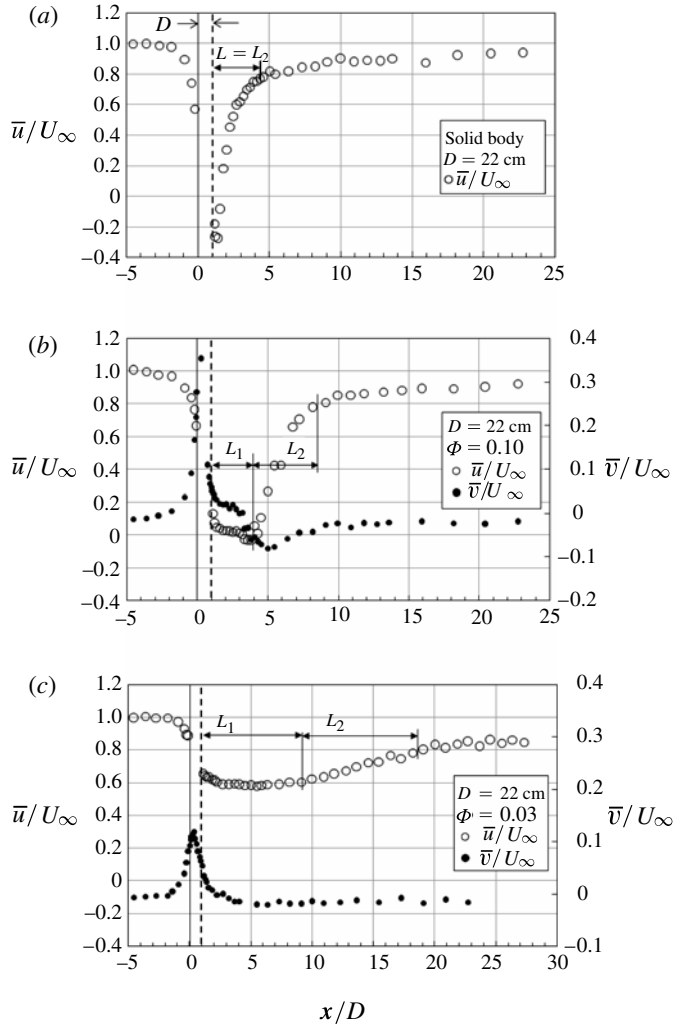


FIGURE 3. Longitudinal profiles of velocity for patches with  $D = 22$  cm: (a) solid body,  $\Phi = 1$ , (b)  $\Phi = 0.10$ , (c)  $\Phi = 0.03$ . Patch is from  $0 < x/D < 1$ . The dashed line indicates the downstream end of the patch. Note that the longitudinal velocity (open circles) is given on the left-hand axis, and the lateral velocity (filled circles) is given on the right-hand axis. The longitudinal velocity ( $\bar{u}$ ) is measured at the centreline,  $y = 0$ . The lateral velocity ( $\bar{v}$ ) is measured at  $y = D/2$ .

$y = D/2$ . For the porous obstructions shown in figures 3(b,c) and 4(b,c), the diversion of flow begins approximately one diameter upstream of the patch, consistent with scaling arguments presented in Rominger & Nepf (2011). For the porous patches the velocity continues to decelerate after entering the patch, as shown by the fact that the velocity measured at the end of the patch ( $x = D$ ) is lower than the velocity entering the patch ( $x = 0$ ). Therefore, flow diversion continues within the patch.

Behind the solid obstruction the wake contains a recirculation zone directly behind the obstruction, shown by the reversed flow ( $\bar{u} < 0$ , figures 3a and 4a), that extends approximately one diameter downstream of the body. After the recirculation zone,  $\bar{u}$  increases rapidly back toward  $U_\infty$ . In principle, the wake can never fully recover,

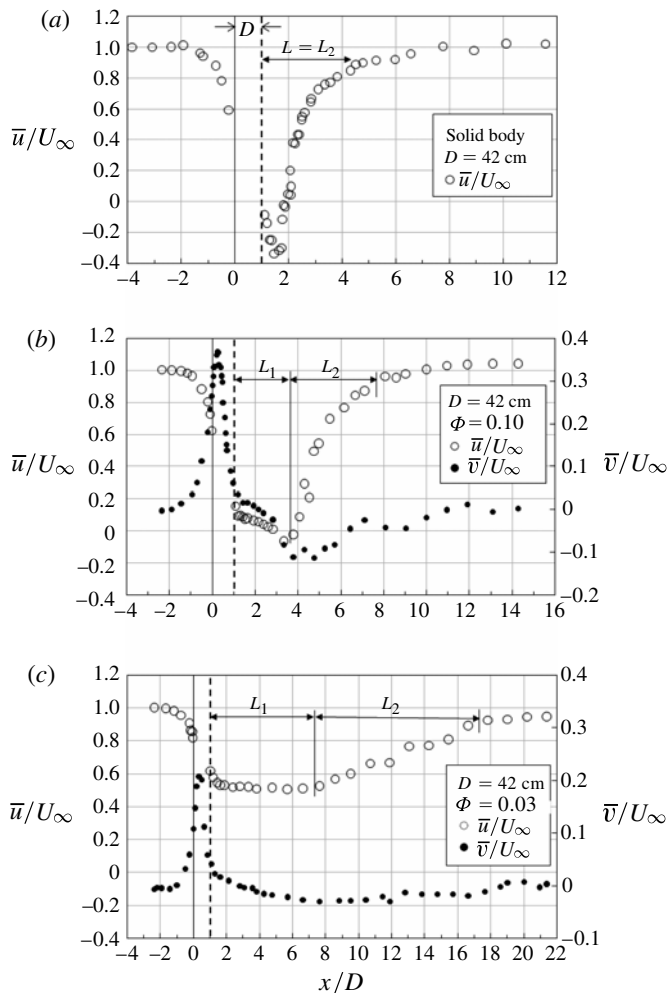


FIGURE 4. Longitudinal profiles of velocity for patches with  $D = 42$  cm: (a) solid body,  $\Phi = 1$ , (b)  $\Phi = 0.10$ , (c)  $\Phi = 0.03$ . Patch is from  $0 < x/D < 1$ . The dashed line indicates the downstream end of the patch. Note that the longitudinal velocity (open circles) is given on the left-hand axis, and the lateral velocity (filled circles) is given on the right-hand axis. The longitudinal velocity ( $\bar{u}$ ) is measured at centreline,  $y = 0$ . The lateral velocity ( $\bar{v}$ ) is measured at  $y = D/2$ .

since the drag-induced momentum deficit must remain constant downstream of the obstruction. However, it is useful to define a total length of the wake,  $L$ , as the distance from the downstream end of the patch ( $x = D$ ) to a point where the rate of velocity recovery is reduced to  $(\partial(\bar{u}/U_\infty))/\partial(x/D) < 0.1$ . For the solid bodies of  $D = 22$  and  $42$  cm,  $L/D = 3.0$  and  $3.3$ , respectively (figures 3a and 4a), and the Reynolds number is  $Re_D = U_\infty D/\nu = 2.2 \times 10^4$  and  $4.1 \times 10^4$ , accordingly. These values are consistent with previous studies. Cantwell & Coles (1983) reported  $L/D = 2.5$  for a cylinder wake at  $Re_D = 1.4 \times 10^5$ . Kravchenko & Moin (1999) numerically studied the flow past a circular cylinder at  $Re_D = 3900$ , and they found  $L/D = 3$ . In contrast, for shallow flows ( $S = C_f D/h > 0.2$ ), the decay scale of the wake is set by the bed friction. Using the e-folding distance defined by Chen & Jirka (1995),  $L = 2h/C_f$ ,



such that the wake length scales with the flow depth, rather than the diameter of the obstruction.

The wakes behind the porous patches are distinct from those behind the solid body. We first consider the porous patch with  $\Phi = 0.03$  and  $D = 22$  cm shown in figure 3(c). Downstream of the patch the velocity continues to decrease, and a diverging flow ( $\bar{v} > 0$ ) is observed until roughly  $x/D \approx 3$ , i.e.  $2D$  beyond the end of the patch. Beyond this point,  $\bar{u}$  is constant until  $x/D = 9$  (figure 3c). This region of uniform velocity is called the steady wake, and the uniform velocity is denoted as  $U_1$ . For the patch with  $\Phi = 0.03$  and  $D = 22$  cm (figure 3c),  $U_1/U_\infty = 0.6$  ( $U_1 = 5.8$  cm s<sup>-1</sup>). In this case, the steady wake extends from the end of the patch ( $x/D = 1$ ) to  $x/D = 9$ , a distance denoted as  $L_1$ . For this case (figure 3c),  $L_1/D = 8$  ( $L_1 = 178$  cm). The magnitudes of  $U_1$  and  $L_1$  for each case are given in table 1. In general, both  $U_1/U_\infty$  and  $L_1/D$  decrease as  $\Phi$  increases, and  $L_1 = 0$  for  $\Phi = 1$  (solid body). For the same  $\Phi$ ,  $L_1$  decreases as  $D$  decreases, but  $U_1/U_\infty$  is not a function of  $D$ . These trends are discussed in greater detail later in the paper.

As the patch becomes denser ( $\Phi$  increases) and  $U_1$  decreases, the diversion of flow increases ( $\bar{v}$  increases). For  $D = 22$  cm, maximum  $\bar{v}/U_\infty$  increases from 0.12 to 0.35 as  $\Phi$  increases from 0.03 to 0.10 (figure 3c,b, respectively, right-hand axes). Similarly, for the cases with  $D = 42$  cm (figure 4c,b), maximum  $\bar{v}/U_\infty$  increases from 0.2 to 0.37 with  $\Phi$  increasing from 0.03 to 0.10.

After the steady wake ( $x > D + L_1$ ), the velocity along the centreline increases, recovering toward the free-stream velocity,  $U_\infty$ . The total length of the wake ( $L$ ) is defined the same way as for the solid body, given above. The wake recovery region has a length scale  $L_2 = L - L_1$  (reported in table 1). For example, in figure 3(c),  $L_2/D = 9.1$  ( $L_2 = 200$  cm), and the total longitudinal extent of the wake is  $L/D = L_1/D + L_2/D = 17.2$  ( $L = 378$  cm). For the solid body case, the region  $L_1$  is absent (i.e.  $L_1 = 0$ ,  $U_1 = 0$ ) and the length of the wake is  $L = L_2$ , which is significantly shorter than the wake of the porous patch of the same size (see table 1, or figures 3 and 4). Further, the spatial acceleration in the wake recovery region declines with decreasing solid volume fraction,  $\Phi$ . The spatial acceleration can be compared using the factor  $(U_\infty - U_1)/L_2$ . For  $D = 22$  cm (figure 3),  $(U_\infty - U_1)/L_2 = 0.15, 0.11, 0.02$  for  $\Phi = 1, 0.10$  and  $0.03$ , respectively. Similarly, for  $D = 42$  cm (figure 4),  $(U_\infty - U_1)/L_2 = 0.07, 0.05, 0.01$  for  $\Phi = 1, 0.10$  and  $0.03$ , respectively. Finally, as the centreline velocity increases over the distance  $L_2$ , continuity requires a mass flux toward the wake centre. This results in a negative transverse velocity ( $\bar{v} < 0$ ) on the line  $y = D/2$ . After  $L_2$ ,  $\bar{v}$  remains small because the velocity deficit in the wake is close to zero.

A flow reversal, indicative of a recirculation zone, is present in the wakes behind the denser patches ( $\Phi = 0.10$  in figures 3b and 4b), but is absent in the wakes of the sparser patches ( $\Phi = 0.03$  in figures 3c and 4c). Specifically,  $\bar{u} < 0$  between  $x/D = 3.2$  and  $3.6$  for  $D = 22$  cm (figure 3b) and between  $3.1$  and  $3.8$  for  $D = 42$  cm (figure 4b). The length of the recirculation zone is a bit smaller for the porous patches than for a solid body, for which the recirculation extended over length scale  $D$ , as discussed above. Castro (1971) observed a recirculation zone behind perforated plates with low porosity ( $\beta = 0$  to  $0.305$ ). For the solid plate ( $\beta = 0$ ), the recirculation zone was attached to the plate. As the porosity increased, the recirculation zone moved downstream. For the highest porosity considered by Castro (1971) ( $\beta = 0.425$ ), no recirculation zone was observed.

Next, we consider the lateral structure of the wake and its evolution downstream. The lateral profiles of  $\bar{u}$  and  $v_{rms}$  for the solid patch of  $D = 22$  cm are shown

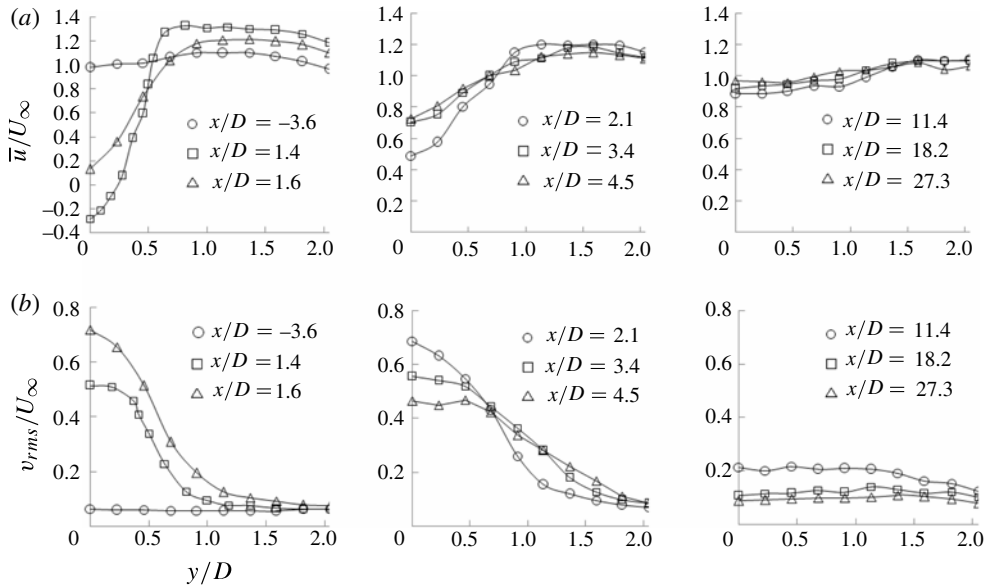


FIGURE 5. Lateral profiles of (a)  $\bar{u}/U_\infty$  and (b)  $v_{rms}/U_\infty$  for the solid circular body with  $D = 22$  cm. Owing to the symmetry about the centreline ( $y/D = 0$ ), measurements were only made on one side of the flume ( $0 < y/D < 2$ ). The solid body is at  $-0.5 < y/D < 0.5$  and  $0 < x/D < 1$ .

in figure 5. One profile taken upstream of the body ( $x/D = -3.6$ ) is included for reference. Behind the solid patch, the velocity deficit,  $(U_\infty - \bar{u}_{y=0})$ , decreases as  $x$  increases. The transverse velocity fluctuation,  $v_{rms}$ , is maximum at the centre of the wake, and decreases monotonically toward the edge of the wake, which is a signature of a vortex street (Townsend 1947; Lyn *et al.* 1995). The maximum value of  $v_{rms}$  at the centreline ( $y/D = 0$ ) decreases with distance downstream, due to the decay of the wake-scale turbulence.

In contrast to the solid body wake, behind the porous patch there is a steady wake region ( $L_1$ ) within which the velocity deficit at the centreline does not change with longitudinal distance (see profiles for  $x/D \leq 9.1$  in figure 6a). Very close to the patch,  $x/D = 1.4$ , the mean velocity across the wake is laterally uniform and lower than the velocity outside the wake ( $y/D > 0.7$ ). At this same position, the turbulence ( $v_{rms}$ ) in the middle of the wake ( $y/D < 0.5$ ) is higher than the level outside the wake (figure 6b). This region of elevated turbulence directly behind the patch is due to the small-scale turbulence generated by individual cylinders. This cylinder-scale turbulence dissipates quickly, disappearing before the next profile at  $x/D = 2.3$  (figure 6b). At  $x/D = 2.3$ , the narrow peak of  $v_{rms}$  at the edge of the wake ( $y/D \approx 0.5$ ) is associated with the shear layer developing between the diminished velocity within the wake and the higher velocity of the free stream. A similar shear layer is present on the opposite side of the wake (not shown). Directly downstream of the patch, the two regions of high shear at the wake's outer edges are separated by the central region of uniform flow (similar to a bleed flow), and the shear layers develop individually with longitudinal distance from the patch. Specifically, the profiles from  $x/D = 1.4$  to  $x/D = 9.1$  in figure 6(a) (i.e. the steady wake region) show a constant velocity at the centre of the wake ( $U_1$ ) and a constant velocity outside the wake ( $U_2$ ), and a shear

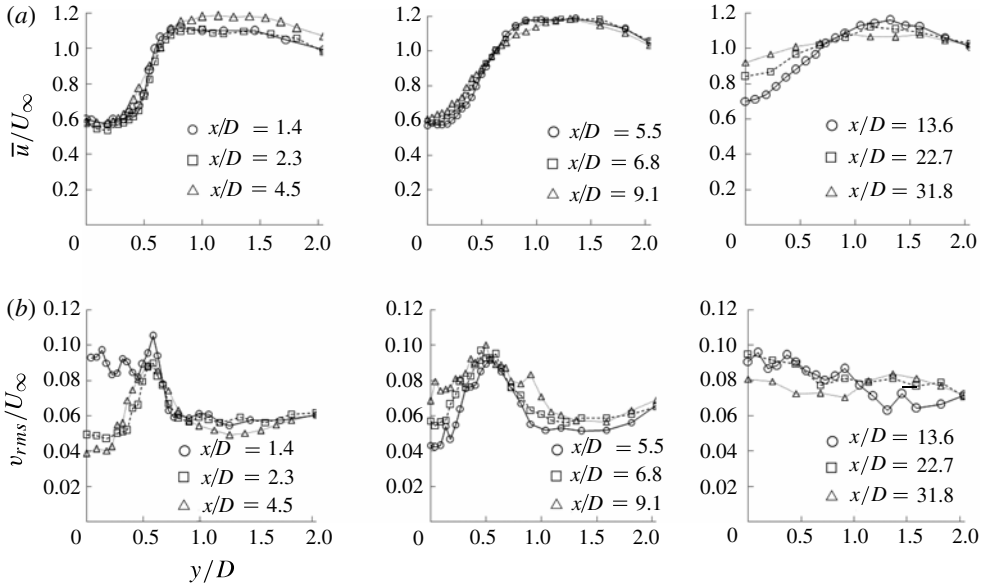


FIGURE 6. Lateral profiles of (a)  $\bar{u}/U_\infty$  and (b)  $v_{rms}/U_\infty$  for the patch of  $D = 22$  cm,  $\Phi = 0.03$ .

region between these limits that grows laterally downstream. The growth of the shear layer can also be seen in the profiles of  $v_{rms}$ , as the peak of  $v_{rms}$  becomes wider, until eventually at  $x/D = 9.1$  the two shear layers merge at the centreline (figure 6b). Beyond  $x/D = 9.1$ , the shear layers interact to form a single von-Kármán vortex street, and  $\bar{u}$  at the centreline starts to increase, due mostly to the enhanced transverse mixing associated with the wake-scale vortices. At  $x/D = 13.6$ ,  $v_{rms}$  is maximum in the middle of the wake, corresponding to a single street of large vortices. Note that the peak  $v_{rms}$  at the centreline is lower for the porous patch (figure 6b) than for the solid body (figure 5b), indicating weaker wake-scale oscillations behind the porous patch. The appearance of the vortices at  $x = D + L_1$  is confirmed by flow visualization, which is discussed below.

In the wake behind a solid body there is a single peak in  $v_{rms}$  at the centreline ( $x/D = 2$ , open circles in figure 7), associated with the formation of the von-Kármán vortex street (Bearman 1965; Lyn *et al.* 1995). In contrast, two distinct zones of elevated turbulence can be identified in the wake behind the porous patch. First, there is a small peak of  $v_{rms}$  directly behind the patch ( $x/D = 1$ , crosses and open squares in figure 7), associated with the small-scale turbulence generated in the wakes of individual cylinders (see also figure 6b,  $x/D = 1.4$ ). These small eddies die out quickly. A second maximum in  $v_{rms}$  appears at the formation of the patch-scale vortices and is denoted as  $v_{rms,max}$ . For  $\Phi = 0.10$  in both figure 7a and figure 7b, the peak ( $v_{rms,max}$ ) at  $x/D = 5$  is nearly as distinct as that behind the solid body. However, as  $\Phi$  decreases (compare  $\Phi = 0.10$  and 0.03 in figure 7),  $v_{rms,max}$  becomes lower, spans a longer longitudinal distance, and moves further downstream. The position and magnitude of  $v_{rms,max}$  are reported in table 1. Note that the position of  $v_{rms,max}$  is measured from the downstream end of the patch. Since the vortex is formed from the interaction of two shear layers, the position of  $v_{rms,max}$  is always downstream of the steady wake region  $L_1$ , consistent with the observation by Wood (1967). Because the turbulence intensity

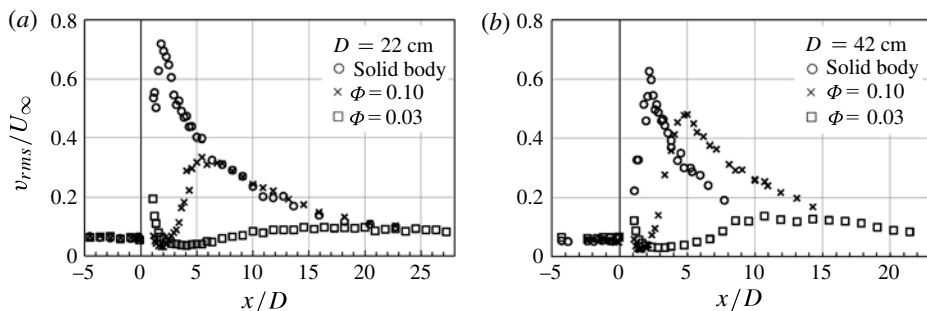


FIGURE 7. Longitudinal profile of  $v_{rms}/U_\infty$  at the centreline,  $y = 0$ : (a)  $D = 22$  cm, (b)  $D = 42$  cm. Patch is at  $0 < x/D \leq 1$ .

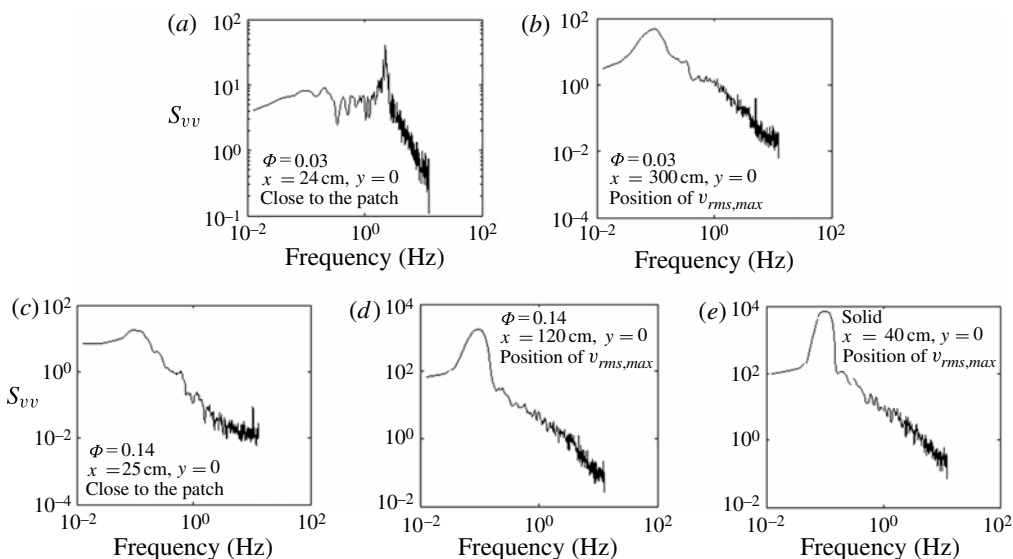


FIGURE 8. Power spectra measured on centreline directly behind the patch (a,c), and at the position of maximum  $v_{rms}$ , (b,d,e). Patch of  $D = 22$  cm and: (a,b)  $\Phi = 0.03$ ; (c,d)  $\Phi = 0.14$ ; (e) solid body.

( $v_{rms,max}$ ) weakens as  $\Phi$  decreases, velocity recovery is slower, i.e.  $L_2/D$  increases as  $\Phi$  decreases (table 1).

The two distinct scales of turbulence present in the wake of the porous patch can be seen in the velocity spectra (figure 8). First consider the patch of  $D = 22$  cm and  $\Phi = 0.03$ . At a location close to the downstream end of the patch ( $x = 24$  cm,  $x/D \approx 1$ , figure 8a), there is a narrow peak in  $S_{vv}$  at  $f_d = 2$  Hz. This corresponds to the von-Kármán vortex street generated behind individual cylinders. Specifically, the cylinder Reynolds number is  $Re_d = (\bar{u}(x = D, y = 0)d)/\nu = 400$ , and its Strouhal number is  $St_d = (f_d d)/\bar{u}(x = D, y = 0) = 0.18$ . This is consistent with the vortex shedding of a solid cylinder,  $St \approx 0.2$  for  $200 < Re < 3 \times 10^5$  (Roshko 1961; Schewe 1983). Further downstream in the same wake ( $x = 300$  cm,  $x/D \approx 14$ , corresponding to the position of  $v_{rms,max}$ , figure 8b), the peak frequency in the spectrum shifts to 0.1 Hz, which

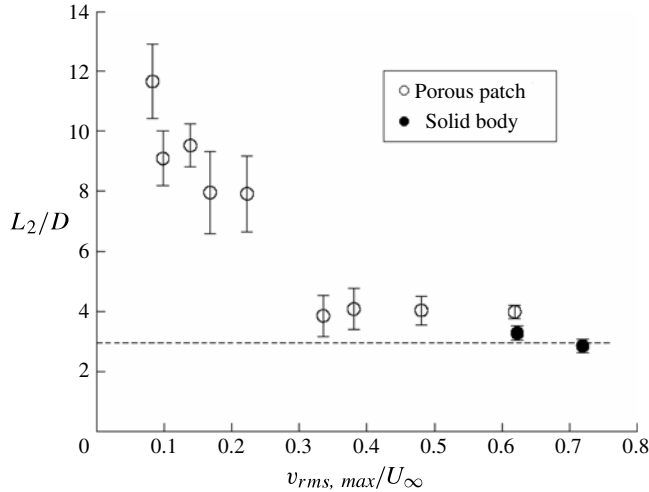


FIGURE 9. The relation between  $L_2/D$  and  $v_{rms,max}/U_\infty$ . The dashed line indicates the solid-body limit.

corresponds to the patch-scale von-Kármán vortex street. In fact, for all patches of diameter  $D = 22$  cm, the velocity spectrum measured at the location of  $v_{rms,max}$  (figure 8*b,d,e*) contained the same dominant frequency,  $f_D = 0.1$  Hz, which corresponds to the shedding frequency of a solid cylinder of diameter  $D = 22$  cm. Specifically,  $St_D = (f_D D)/U_2 = 0.17$ . Note that  $U_2$  is used instead of  $U_\infty$ , as a more representative value for the outer shear-layer velocity. By comparing the magnitude of the peaks in  $S_{vv}$  (figure 8*b,d,e*), we note that the turbulence intensity of the wake-scale vortices is greatest for the solid body (figure 8*e*,  $S_{vv} = O(10^4)$ ), and decreases with solid volume fraction. Specifically, the peak is higher for the denser patch shown (figure 8*d*,  $S_{vv} = O(10^3)$ ) than for the sparser patch shown (figure 8*b*,  $S_{vv} = O(10^2)$ ), which is consistent with the turbulence profiles shown in figure 7, i.e.  $v_{rms,max}$  is smaller for smaller  $\Phi$  (larger porosity). For the case of  $D = 22$  cm and  $\Phi = 0.14$ , the velocity exiting the patch is too low to generate cylinder-scale turbulence,  $Re_d = O(10)$ ; therefore there is no velocity fluctuation at the cylinder scale for this case, i.e. no peak in spectrum (figure 8*c*).

After the two shear layers grow wide enough to interact and form a von-Kármán vortex street, the velocity in the wake starts to increase. The length of the velocity recovery (wake decay) region is  $L_2$ . The increase of the centreline velocity back to the free-stream value is due to the cross-wake mixing driven by the wake-scale vortex street. The turbulence intensity is less for the porous body than for the solid body (figure 7) and consequently the length scale required for the velocity to recover ( $L_2$ ) is longer for the porous body wakes, compared to the solid body case (figure 9). Specifically,  $L_2/D$  increases with decreasing  $v_{rms,max}$ . The solid body cases (shown as solid symbols) indicate that the lower limit of  $L_2/D$  is 3 (dashed line).

### 3.2. Flow visualization

Flow visualization was used to observe both the steady wake and the vortex street (figure 10). Images are grouped by patch size,  $D$ . For each patch size, the steady wake becomes longer and the lateral extent of the wake oscillation becomes smaller as  $\Phi$  decreases. The distance from the downstream end of the patch to the point

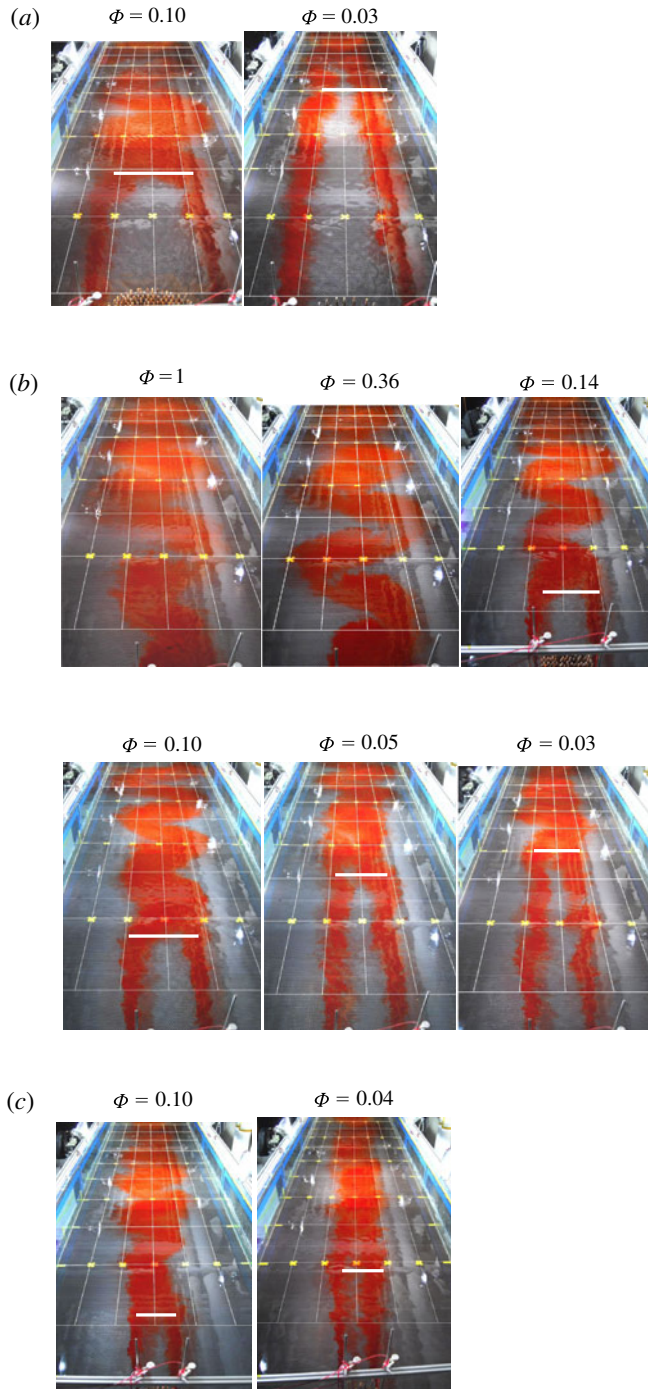


FIGURE 10. Flow visualization. The patch is just out of sight at the bottom of each picture. Flow is from bottom to top. The dye was injected at the two outmost edges of the patch. The struts holding the dye injector are visible in some of the pictures. The white grid starts at  $x = 50$  cm (from the leading edge of the patch) and marks the distance of 50 cm in the  $x$ -direction and 20 cm in the  $y$ -direction. The yellow crosses mark 1 m intervals. The horizontal white bar indicates the end of the steady wake ( $L_{1,dye}$ ). The values of  $L_{1,dye}$  are reported in table 1. (a)  $D = 42$  cm; (b)  $D = 22$  cm; (c)  $D = 12$  cm.



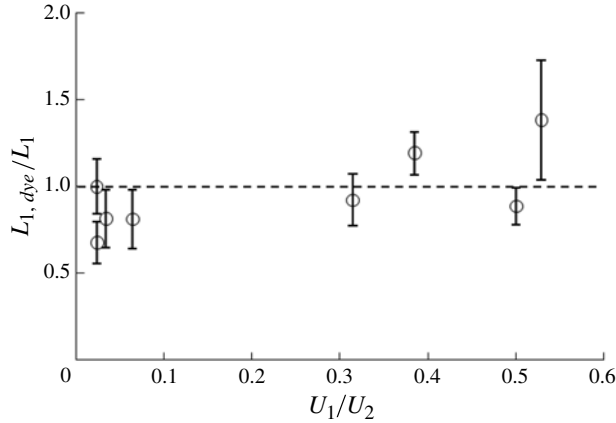


FIGURE 11. Comparison between  $L_1$  and  $L_{1,dye}$ .  $L_1$  is the length of the steady wake measured from longitudinal profile of  $\bar{u}$  at the centreline.  $L_{1,dye}$  is measured from flow visualization, and is defined as the point at which the dye traces meet at the centreline.

where the two streaks of dye merge, denoted  $L_{1,dye}$ , is another measure of the steady wake region. For each case,  $L_{1,dye}$  was obtained by averaging the lengths measured from ten individual pictures (table 1). The length scales of the steady wake region measured from velocity profiles ( $L_1$ ) and from dye images ( $L_{1,dye}$ ) are the same within uncertainty (figure 11).

Because pictures were taken at 2 s intervals, the vortex frequency ( $f_D$ ) could be estimated from the picture series. The images also reveal that the vortices become increasingly irregular and intermittent as the solid volume fraction decreases. For example, in the case of  $D = 12$  cm,  $\Phi = 0.04$  (figure 10c), the two dye streaks eventually mix downstream, but no clear pattern of oscillation occurs. Similarly, in Castro's (1971) study of the wake behind a perforated plate, the vortex street ceases to form for the plates with porosity higher than 0.2, which is a solid volume fraction  $\Phi < 0.8$ . For the porous array considered here, the transition occurs at a much lower  $\Phi$ , with the vortex street ceasing to form only for  $\Phi < 0.04$ . This is very close to the limit ( $\Phi = 0.05$ ) found with the numerical model of Nicolle & Eames (2011). The higher solid volume fraction limit observed by Castro (1971) is likely to be associated with the difference in aspect ratio between a slim plate, with streamwise dimension much smaller than spanwise dimension (Castro 1971), and a circular patch, with comparable streamwise and spanwise dimensions (Nicolle & Eames 2011, and the present study). The cessation of the vortex street at some level of porosity is related to the velocity difference induced by the porous obstruction. As the porosity increases, the velocity difference  $U_2 - U_1$  decreases, producing a smaller velocity gradient. When  $U_2 - U_1$  is too small, the instability is not strong enough to generate a vortex street, although weak oscillations may still be identified in spectral analysis, a phenomenon Castro (1971) referred to as wake flapping.

The Strouhal number,  $St_D = f_D D / U_2$ , based on the frequency obtained by flow visualization, is included in table 1. The values of  $f_D$  found through imaging agree with the spectral peak estimates, also shown in table 1. A distinct vortex street is observed for  $U_1 / U_2 < 0.35$  ( $\Phi > 0.04$ ), and no vortex street is observed for  $U_1 / U_2 > 0.35$  ( $\Phi < 0.04$ , figure 12). For cases without a visual vortex street, oscillation was still picked up in the spectra. Whether or not a vortex street was observed,  $St_D$  estimated from spectra was nearly constant with a mean value of 0.17.



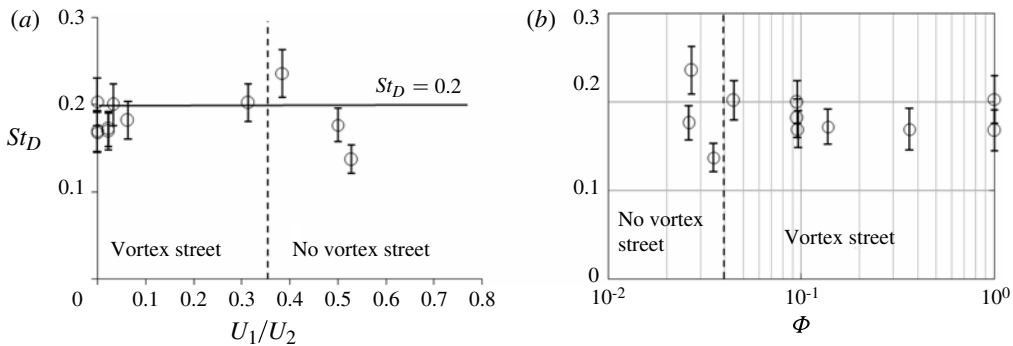


FIGURE 12. Strouhal number ( $St_D = f_D D/U_2$ ) versus (a) the velocity ratio of  $U_1/U_2$  and (b) solid volume fraction. The existence of a vortex street is determined from the flow visualization. For the cases with the vortex street,  $f_D$  is obtained from the flow visualization. For the cases with no vortex street,  $f_D$  is obtained from  $S_{vv}$ .

This is similar to the results of Ball *et al.* (1996), who observed  $St_D = 0.22$  for  $\Phi = 0.23, 0.06$  and  $0.01$ . In contrast, Castro (1971) recorded a gradual, but distinct, upward shift in Strouhal number as the solid volume fraction of their perforated plate decreased. This may be attributed to a shift in the shedding length scale from the plate width to the smaller length scales defined by the solid material between the holes in the plate. A similar shift was observed by Nicolle & Eames (2011). Specifically, for low solid volume fractions ( $\Phi < 0.05$ ) the shedding from individual cylinders within the patch determined the oscillation frequency in the near wake, i.e. the individual cylinder diameter set the length scale for vortex shedding. However, for higher solid volume fraction, the patch behaved like a solid array, producing wake oscillations that scaled on the patch diameter. Because the spectral analysis for figure 12 is made further downstream from the obstruction than these two previous studies, it does not reflect the oscillations associated with individual cylinders within the patch (e.g. as observed in spectra directly behind the patch, figure 8a), and this might explain why we do not see an increase in oscillation frequency as the patch solid volume fraction decreases.

Finally, the porosity not only has an impact on the velocity difference  $\Delta U = U_2 - U_1$ , but also the efficiency with which this shear is converted to turbulence. Specifically, the ratio  $v_{rms}/\Delta U$  decreases with decreasing  $\Phi$  (i.e. increasing porosity), as shown in figure 13. This is consistent with changes in the vortex strength and coherence observed by flow visualization. Note that  $\Phi = 0.4$  is close to the solid body limit  $v_{rms,max}/\Delta U = 0.5$ . In addition, since  $v_{rms,max}$  is positively related to the velocity difference,  $\Delta U$  (figure 13), and the wake decay depends on the turbulence intensity in the wake (shown in figure 9),  $L_2$  increases with increasing  $U_1/U_2$ . Figure 14 shows this trend of  $L_2/D$  and  $L/D$  increasing with increasing  $U_1/U_2$ . The solid body cases correspond to  $U_1/U_2 = 0$  and  $L/D = L_2/D \approx 3$ .

## 4. Discussion

### 4.1. Steady wake region and growth of the shear layer ( $L_1$ )

In the steady wake behind the porous patch, shear layers at the two wake edges grow until they meet at the middle of the wake, after which a single vortex street can form.

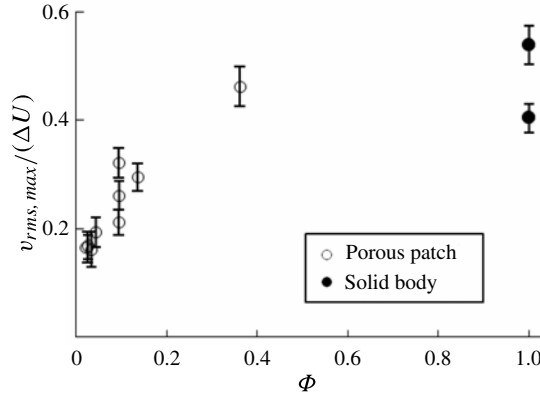


FIGURE 13. Turbulence intensity,  $v_{rms,max}$ , normalized by the velocity difference  $\Delta U = U_2 - U_1$ .

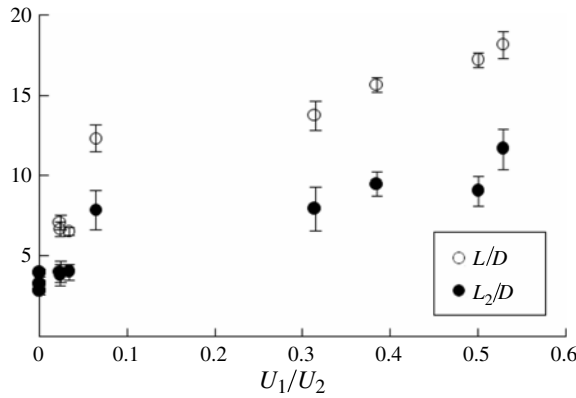


FIGURE 14.  $L_2/D$  and  $L/D$  versus the velocity ratio of  $U_1/U_2$ .

The length of the steady wake,  $L_1$ , is therefore determined by the growth rate of the individual shear layers and the patch diameter, which sets the initial distance between the shear layers. We draw on previous descriptions of planar shear layer growth (e.g. Champagne, Pao & Wygnanski 1976). The characteristic width of the shear layer is  $\delta$  (figure 15a). Given the mean velocity within the shear layer,  $\bar{U}$ , and the velocity difference,  $\Delta U$ , the shear layer growth rate is

$$\frac{d\delta}{dx} = S_\delta \frac{\Delta U}{\bar{U}}; \quad (4.1)$$

$S_\delta$  is an empirical parameter which is constant over a wide range of  $\Delta U/\bar{U}$ . Dimotakis (1991) reports  $S_\delta \approx 0.06$  to  $S_\delta \approx 0.11$ . Champagne *et al.* (1976) found  $S_\delta \approx 0.097$ . The shear layer grows linearly and preferentially into the low-velocity stream (figure 15b). The length scale  $\delta$  is the distance between the positions of  $y_{0,9}$  and  $y_{0,1}$ . In this study we are only interested in how fast the shear layers grow toward the centre of the wake, and at what  $x$  position they reach the centreline, so that we are only interested in the position of  $y_{0,1}$ . We define a new width,  $\delta_1$ , as the distance from the edge of the patch,  $y = D/2$ , to  $y_{0,1}$  (figure 16). Using a formula similar to (4.1),  $S_{\delta_1}$  is the growth

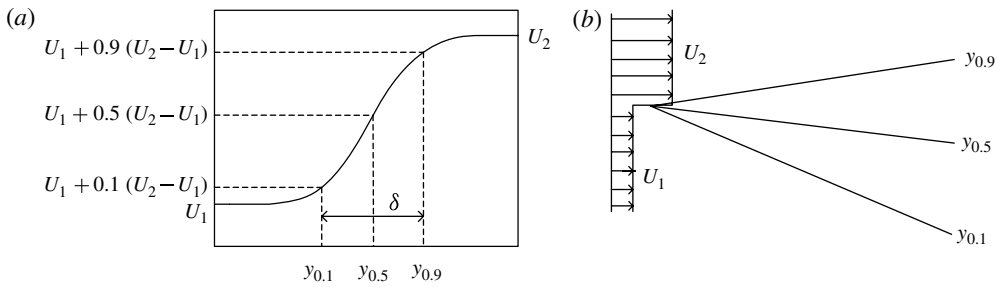


FIGURE 15. The plane shear layer. (a) Definition of shear layer width,  $\delta = y_{0.9} - y_{0.1}$ . (b) Streamwise variations of  $y_{0.1}$ ,  $y_{0.5}$  and  $y_{0.9}$ .

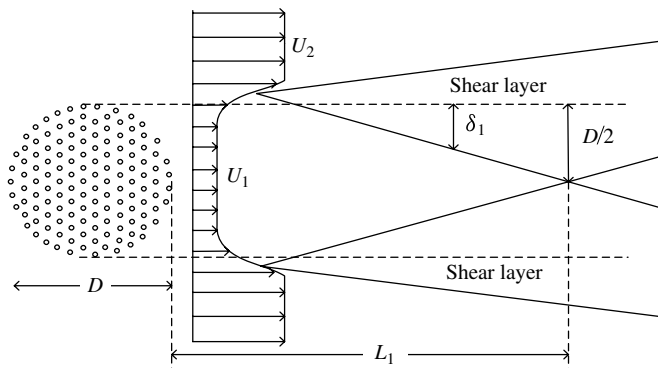


FIGURE 16. Sketch of the shear layer growth in  $L_1$ , and the definition of  $\delta_1$ .

parameter for  $\delta_1$ . The low velocity within the steady wake is  $U_1$  and the velocity outside the wake is  $U_2$ , such that  $\bar{U} = (U_1 + U_2)/2$  and  $\Delta U = U_2 - U_1$ . Rearranging (4.1),  $S_{\delta_1}$  can be obtained from  $d\delta_1/dx$ ,

$$S_{\delta_1} = (d\delta_1/dx)(\bar{U}/\Delta U). \tag{4.2}$$

Lateral profiles of Reynolds stress  $(\overline{u'v'})$  within the steady wake region were used to estimate  $d\delta_1/dx$ . For example, figure 17(a) shows the lateral profiles of Reynolds stress for the patch of  $D = 42$  cm,  $\Phi = 0.03$ . In each profile, the region of negative Reynolds stress corresponds to the shear layer. We define the inner edge of the shear layer as the point where the Reynolds stress reaches zero. Then,  $\delta_1$  is the distance from the inner edge of the shear layer to the edge of the patch ( $y = D/2$ ). An example is shown in figure 17(a). The length scale,  $\delta_1$ , measured for each profile (figure 17a) is shown in figure 17(b), from which  $d\delta_1/dx = 0.089 \pm 0.008$ . With  $U_1 = 5.0$  cm s<sup>-1</sup> and  $U_2 = 13.0$  cm s<sup>-1</sup> (table 1), we obtained,  $S_{\delta_1} = 0.098 \pm 0.014$  from (4.2). The values of  $S_{\delta_1}$  obtained for all cases, and the corresponding values of  $\bar{U}/\Delta U$  are plotted in figure 18. There is no clear trend between  $S_{\delta_1}$  and  $\bar{U}/\Delta U$ , so that we can assume  $S_{\delta_1} = 0.10 \pm 0.02$  is a constant. Using this value,  $L_1$  can be estimated from the modified equation (4.2),  $d\delta_1/dx = S_{\delta_1}\Delta U/\bar{U}$ . The length scale  $L_1$  extends from  $x = D$  to a point where

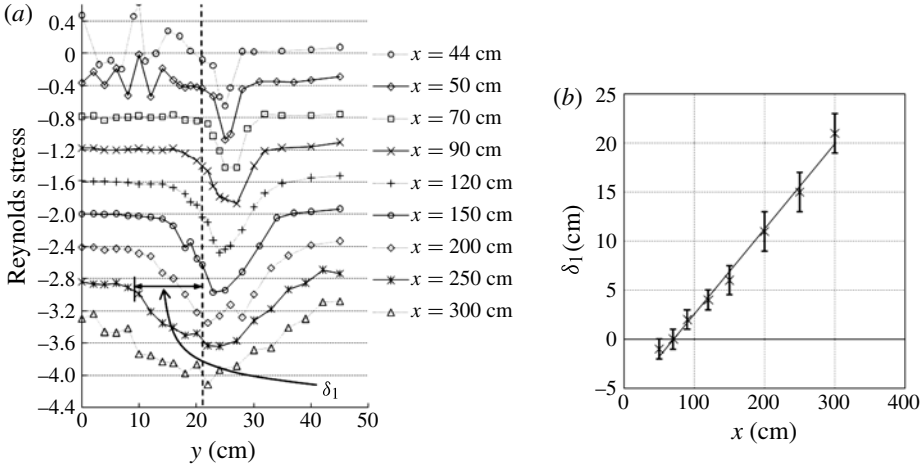


FIGURE 17.  $D = 42$  cm and  $\Phi = 0.03$ . (a) The lateral profiles of Reynolds stress. Each profile is offset by  $-0.4$  from the previous profile.  $\delta_1$  is measured from the edge of the patch (dashed line,  $y = D/2 = 21$  cm) to the inner edge of the negative peak of the Reynolds stress. As an example, the width estimated for the  $x = 250$  cm profile is indicated. (b) The width of the shear layer,  $\delta_1$ , as a function of  $x$ . The slope and its uncertainty are obtained by linear regression with 95% confidence level,  $d\delta_1/dx = 0.089 \pm 0.008$ .

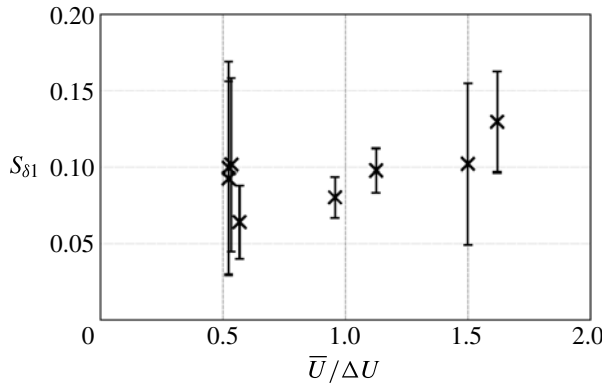


FIGURE 18. The values of  $S_{\delta_1}$  determined from (4.2) versus  $\bar{U}/\Delta U$ .

$\delta_1 = D/2$ ; therefore, assuming  $\delta_1 = 0$  at  $x = D$ ,  $d\delta_1/dx = (D/2)/L_1$ , so we can write

$$L_1 \approx \frac{D/2}{S_{\delta_1}} \frac{\bar{U}}{\Delta U}. \quad (4.3)$$

The values of  $L_1$  predicted from (4.3) agree with the measured values within uncertainty (figure 19).

Wood (1967) and Ball *et al.* (1996) also studied the steady wake region using flow visualization. In Wood's experiment, particles were introduced into the channel flow but not into the base bleed flow. A clear region with no particles was observed directly behind the body. It indicated that the bleed flow did not mix with the outside flow for some distance behind the trailing edge,  $L_{Wood}$ , which has similar meaning to our  $L_1$ . Wood (1967) found that  $L_{Wood}$  increased as the velocity ratio  $U_1/U_2$  increased,

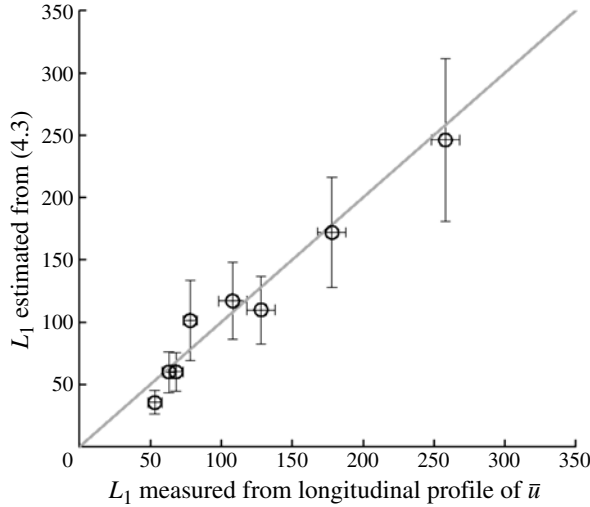


FIGURE 19. Comparison between  $L_1$  measured from longitudinal profiles of  $\bar{u}$  and  $L_1$  calculated from (4.3).

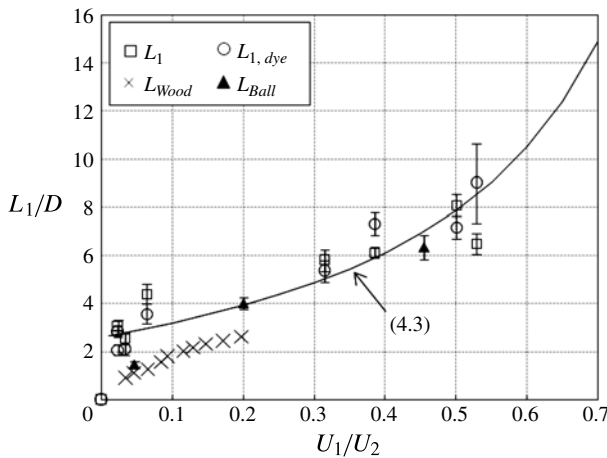


FIGURE 20. The relation between the dimensionless length of the steady wake,  $L_1/D$ , and the velocity ratio  $U_1/U_2$ . The estimated value of  $L_1$  from (4.3) is represented by the solid line.

where  $U_1$  was the bleed flow rate and  $U_2$  was the velocity outside the wake. Ball *et al.* (1996) injected dye at the centre of the upstream face of a square array of circular cylinders and the dye streak remained straight until some distance behind the array,  $L_{Ball}$ , and then started to oscillate laterally. In our study, we injected dye at two sides of the circular array of circular cylinders. Similar to Wood's cases, a clear region behind the porous array is observed and its length is denoted as  $L_{1,dye}$  (table 1). The several observations of  $L_1$  ( $L_{Wood}$ ,  $L_{Ball}$ ,  $L_{1,dye}$ ,  $L_1$ ) are compared to the prediction of  $L_1$  (from (4.3)) in figure 20. A data point at  $L_1/D = 0$  and  $U_1/U_2 = 0$  represents the bluff body case which has no region  $L_1$ . All three studies show the same trend: dimensionless length,  $L_1/D$ , increases as  $U_1/U_2$  increases.  $L_{Ball}$  is close to our data.  $L_{Wood}$  has the same slope but is offset from the other studies by about  $D$ . The possible

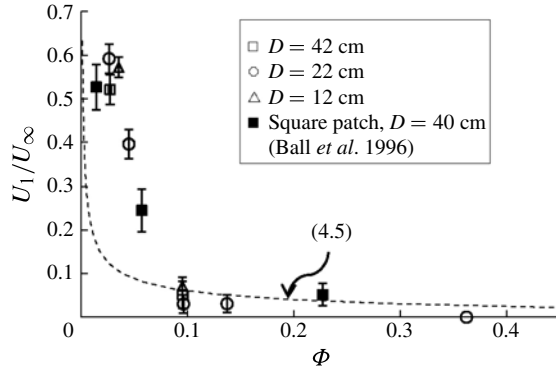


FIGURE 21. Velocity in the steady wake region ( $U_1$ ) as a function of the cylinder density ( $\Phi$ ). The estimation from (4.5) is represented as a solid line.

reason is that Wood's model is more streamlined, and in particular has a greater aspect ratio (length to width), so that the flow directly at the trailing edge is a parallel shear layer. However, in Ball's study and in the current study, the patch has an aspect ratio of 1, so that the flow at the trailing edge is not parallel, and additional flow diversion is observed after the body, extending about one diameter downstream from the body. Thus, for obstructions of aspect ratio 1, a parallel flow shear layer may not be achieved until one diameter downstream of the trailing edge, and this lengthens the steady wake by one diameter, consistent with the shift between Wood's measurements and the other studies (figure 20).

#### 4.2. Magnitude of flow in the steady wake region ( $U_1$ )

The reduction in velocity from  $U_\infty$  to  $U_1$  depends on the drag imposed by the patch, which is related to both the size of the patch ( $D$ ) and its solid volume fraction ( $\Phi$ ). However, in the cases considered here,  $U_1/U_\infty$  depends only on  $\Phi$ , and is independent of  $aD$  (figure 21). The square patches tested by Ball *et al.* (1996) are also included in figure 21. For the patch  $\Phi = 0.36$ ,  $U_1/U_\infty$  is essentially zero, within measurement uncertainty, suggesting that the solid body limit has been reached by this value of  $\Phi$ .

The lack of dependence on  $aD$  can be explained by results from Rominger & Nepf (2011), who describe the deceleration through a long porous patch (length much larger than width). The velocity at the centreline starts to decline from some distance upstream of the patch, and the deceleration continues into the patch over a length  $x_D$ , after which the flow reaches a steady velocity,  $U_0$ . Rominger & Nepf (2011) found that the upstream adjustment length scales on the half-width of the patch ( $b = D/2$ ), and both the interior adjustment length ( $x_D$ ) and the final interior velocity ( $U_0$ ) depend on the dimensionless parameter,  $C_D aD$ , called the patch flow-blockage.  $C_D$  is the drag coefficient for the cylinders within the patch. Adapting (4.2) from Rominger & Nepf (2011), the interior adjustment length scale is given by

$$\frac{x_D}{D} \sim \frac{2}{C_D aD} \left[ 1 + \left( \frac{C_D aD}{4} \right)^2 \right]^{1/2}. \quad (4.4)$$

For low flow blockage ( $C_D aD < 4$ ),  $x_D/D$  scales with  $(C_D aD)^{-1}$ . For high flow blockage ( $C_D aD > 4$ ),  $x_D \sim D$  only. Using  $C_D = 1$  for simplicity,  $C_D aD = 0.8$ –17 for the patches tested in this paper. Specifically, for all cases with  $\Phi \geq 0.1$ ,  $C_D aD > 4$ ,

and these cases fall in the high-flow-blockage regime and therefore  $x_D \sim D$ . If the patches were infinitely long, the flow would adjust to its interior velocity over the length scale  $D$ . The circular patches we studied provide just this length, so  $U_1$  is expected to be equal to the interior velocity predicted for an infinite patch ( $U_1 = U_0$ ), which was derived by Rominger & Nepf (2011),

$$\frac{U_0}{U_\infty} = \sqrt{\frac{C_f (1 - \Phi)}{h C_D a}} = \sqrt{\frac{C_f d}{C_D h} \left( \frac{1}{\Phi} - 1 \right)}. \tag{4.5}$$

Note that in this regime  $U_0/U_\infty$  is a function only of the solid volume fraction, consistent with our observations ( $U_1/U_\infty = f(\Phi)$ , figure 21). The velocity predicted from (4.5), using the previously measured  $C_f = 0.006$ , the drag coefficient,  $C_D = 1$ , cylinder diameter,  $d = 0.6$  cm, and the water depth,  $h = 13.3$  cm, is shown with a dashed line in figure 21. The agreement with the experimental results is excellent for  $\Phi \geq 0.1$ , for which  $C_D a D \geq 4$ , consistent with the definition of high flow blockage.

In the low-flow-blockage regime ( $C_D a D < 4$ ), the interior adjustment length scales with  $(C_D a)^{-1}$ , (4.4), which is longer than  $D$ . In that case, the near-wake velocity would be higher than the interior velocity predicted by (4.5), and we would expect the normalized velocity,  $U_1/U_\infty$ , to be a function of the flow blockage ( $aD$ ) as well as the solid volume fraction ( $\Phi$ ). Indeed, at the lowest patch density considered here ( $\Phi = 0.03, 0.04, C_D a D = 0.8\text{--}2.5$ ) the measured velocity is higher than the prediction from (4.5) as shown in figure 21. Finally, for  $\Phi \leq 0.1$ , the channel blockage did not have an impact on  $U_1/U_\infty$ . Specifically, at both  $\Phi = 0.1$  and  $0.03$ ,  $U_1$  for all three blockages ( $D/B = 0.10, 0.18, 0.35$ ) agreed within uncertainty (figure 21). However, we expect  $U_1/U_\infty$  will be dependent on  $D/B$  at higher values of channel flow blockage, specifically as  $D/B$  approaches unity.

### 5. Conclusion

The wake behind a porous body has two unique features compared to the wake behind a solid body. First, a steady wake region extends a distance  $L_1$  behind the body, and  $L_1$  increases with increasing patch porosity. Second, the formation of the von-Kármán vortex street is delayed until beyond  $L_1$ . The flow exiting the patch is laterally uniform and slower than the flow that passes around the patch. The streamwise velocity at the centreline ( $U_1$ ) remains at a constant value over the majority of the steady wake region. For the patch diameters and porosities considered here,  $U_1/U_\infty$  is a function of the porosity only. Close behind the patch, the wake contains small-scale turbulence generated in the wakes of individual cylinders. Shear layers form at both sides of the wake. Initially, the two shear layers do not interact, and grow independently with distance downstream from the patch. The shear layers grow to the centreline at  $x = D + L_1$ , which marks the end of the steady wake. The length of the steady wake region ( $L_1$ ) can be predicted using the equation of the plane shear layer growth.

After the steady wake ( $L_1$ ), a von-Kármán vortex street is formed from the interaction between the shear layers. The turbulence structure in this region is on the scale of the patch and dominates the transverse mixing across the wake. The maximum turbulence intensity behind a patch ( $v_{rms,max}$ ) is lower than that behind a solid body, which leads to a slower decay of the velocity deficit. As the solid volume fraction decreases, and  $U_1/U_2$  increases, the vortex street weakens, losing some coherence, and for  $\Phi < 0.04$ , no vortex street is formed and only weak oscillation exists in the wake.



### Acknowledgements

This material is based upon work supported by a NSF Grant, EAR 0738352. Any opinions, conclusions or recommendations expressed in this material are those of the authors and do not necessarily reflect the views of the National Science Foundation. We thank M. O'Donnell and T. Cheng for their assistance with the experiments. T. Cheng was supported by MIT's P. Grey Fund for undergraduate research.

### REFERENCES

- BALL, D. J., STANSBY, P. K. & ALLISTON, N. 1996 Modelling shallow water flow around pile groups. *Proc. Inst. Civ. Engrs Wat., Marit. Energy* **118**, 226–236.
- BEARMAN, P. W. 1965 Investigation of the flow behind a two-dimensional model with a blunt trailing edge and fitted with splitter plates. *J. Fluid Mech.* **21** (2), 241–255.
- BOUMA, T., VAN DUREN, L., TEMMERMAN, S., CLAVERIE, T., BLANCO-GARCIA, A., YSEBAERT, T. & HERMAN, P. 2007 Spatial flow and sedimentation patterns within patches of epibenthic structures: combining field, flume and modelling experiments. *Cont. Shelf Res.* **27**, 1020–1045.
- BROOKSHIRE, E. & DWIRE, K. 2003 Controls on patterns of coarse organic particle retention in headwater streams. *J. N. Am. Benth. Soc.* **22**, 17–34.
- CANTWELL, B. & COLES, D. 1983 An experimental study of entrainment and transport in the turbulent near wake of a circular cylinder. *J. Fluid Mech.* **136**, 321–374.
- CASTRO, I. P. 1971 Wake characteristics of two-dimensional perforated plates normal to an air-stream. *J. Fluid Mech.* **46** (3), 599–609.
- CHAMPAGNE, F. H., PAO, Y. H. & WYGNANSKI, I. J. 1976 On the two-dimensional mixing region. *J. Fluid Mech.* **74**, 209–250.
- CHEN, D. & JIRKA, G. H. 1995 Experimental study of plane turbulent wakes in a shallow water layer. *Fluid Dyn. Res.* **16**, 11–41.
- CHEN, J. H., PRITCHARD, W. H. & TAVENER, S. J. 1995 Bifurcation for flow past a cylinder between parallel planes. *J. Fluid Mech.* **284**, 23–41.
- COTTON, J., WHARTON, G., BASS, J., HEPPELL, C. & WOTTON, R. 2006 The effects of seasonal changes to in-stream vegetation cover on patterns of flow and accumulation of sediment. *Geomorphology* **77**, 320–334.
- COUTANCEAU, M. & BOUARD, R. 1977 Experimental determination of the main features of the viscous flow in the wake of a circular cylinder in uniform translation. Part 1. Steady flow. *J. Fluid Mech.* **79**, 231–256.
- DIMOTAKIS, P. E. 1991 Turbulent free shear layer mixing and combustion. In *High-Speed Flight Propulsion Systems* (ed. S. N. B. Murthy & E. T. Curran), pp. 265–340. AIAA.
- FONSECA, M., ZIEMAN, J., THAYER, G. & FISHER, J. 1983 The role of current velocity in structuring eelgrass meadows. *Estuar. Coast. Shelf Sci.* **17**, 367–380.
- GACIA, E. & DUARTE, C. 2001 Sediment retention by a Mediterranean *Posidonia oceanica* meadow: the balance between deposition and resuspension. *Estuar. Coast. Shelf. Sci.* **52** (4), 505–514.
- HUANG, Z. & KEFFER, J. F. 1996 Development of structure within the turbulent wake of a porous body. Part 1. The initial formation region. *J. Fluid Mech.* **329**, 103–115.
- KRAVCHENKO, A. G. & MOIN, P. 1999 Numerical studies of flow over a circular cylinder at  $Re_D = 3900$ . *Phys. Fluids* **12** (2), 403–417.
- LOPEZ, F. & GARCIA, M. 1998 Open-channel flow through simulated vegetation: suspended sediment transport modelling. *Water Resour. Res.* **34** (9), 2341–2352.
- LYN, D. A., EINAV, S., RODI, W. & PARK, J.-H. 1995 A laser-Doppler velocimetry study of ensemble-averaged characteristics of the turbulent near wake of a square cylinder. *J. Fluid Mech.* **304**, 285–319.
- MOORE, K. A. 2004 Influence of seagrasses on water quality in shallow regions of the lower Chesapeake bay. *J. Coast. Res.* **20**, 162–178 (special issue).
- NEPF, H. 1999 Drag, turbulence and diffusivity in flow through emergent vegetation. *Water Resour. Res.* **35** (2), 479–489.

- NICOLLE, A. & EAMES, I. 2011 Numerical study of flow through and around a circular array of cylinders. *J. Fluid Mech.* **679**, 1–31.
- NORBERG, C. 1994 An experimental investigation of the flow around a circular cylinder: influence of aspect ratio. *J. Fluid Mech.* **258**, 287–316.
- ROMINGER, J., LIGHTBODY, A. & NEPF, H. 2010 The effects of added vegetation on sand bar stability and stream hydrodynamics. *J. Hydraul. Engng* **136** (12), 944.
- ROMINGER, J. & NEPF, H. 2011 Flow adjustment and interior flow associated with a rectangular porous obstruction. *J. Fluid Mech.* **680**, 636–659.
- ROSHKO, A. 1961 Experiments on the flow past a circular cylinder at very high Reynolds number. *J. Fluid Mech.* **10**, 345–356.
- SAHIN, M. & OWENS, R. G. 2004 A numerical investigation of wall effects up to high blockage ratios on two-dimensional flow past a confined circular cylinder. *Phys. Fluids* **16** (5), 1305–1320.
- SAND-JENSEN, K. & PEDERSEN, M. L. 2008 Streamlining of plant patches in streams. *Freshwat. Biol.* **53**, 714–726.
- SCHEWE, G. 1983 On the force fluctuation acting on a circular cylinder in cross-flow from subcritical up to transcritical Reynolds numbers. *J. Fluid Mech.* **133**, 265–285.
- SCHULTZ, M., KOZERSKI, H.-P., PLUNTKE, T. & RINKE, K. 2003 The influence of macrophytes on sedimentation and nutrient retention in the lower river spree. *Water Resour. Res.* **37**, 569–578.
- SHARPE, R. G. & JAMES, C. S. 2006 Deposition of sediment from suspension in emergent vegetation. *Water SA* **32** (2), 211–218.
- STONE, B. & SHEN, H. T. 2002 Hydraulic resistance of flow in channels with cylindrical roughness. *J. Hydraul. Engng ASCE* **128** (5), 500–506.
- TAKEMURA, T. & TANAKA, N. 2007 Flow structures and drag characteristics of a colony-type emergent roughness model mounted on a flat plate in uniform flow. *Fluid Dyn. Res.* **39**, 694.
- TANINO, Y. & NEPF, H. 2008 Lateral dispersion in random cylinder arrays at high Reynolds number. *J. Fluid Mech.* **600**, 339–371.
- TOWNSEND, A. A. 1947 Measurements in the turbulent wake of a cylinder. *Proc. R. Soc. Lond. A* **190**, 551–561.
- TURKI, S., ABBASSI, H. & NASRALLAH, S. B. 2003 Effect of the blockage ratio on the flow in a channel with a built-in square cylinder. *Comput. Mech.* **33**, 22–29.
- WHITE, B. & NEPF, H. 2007 Shear instability and coherent structures in a flow adjacent to a porous layer. *J. Fluid Mech.* **593**, 1–32.
- WHITE, B. & NEPF, H. 2008 A vortex-based model of velocity and shear stress in a partially vegetated shallow channel. *Water Resour. Res.* **44**, W01412.
- WINDHAM, L., WEIS, J. & WEIS, P. 2003 Uptake and distribution of metals in two dominant salt marsh macrophytes, *Spartina alterniflora* and *Phragmites australis*. *Estuar. Coast. Shelf Sci.* **56**, 63–72.
- WIDDOWS, J., POPE, N. & BRINSLEY, M. 2008 Effect of *Spartina anglicastems* on near-bed hydrodynamics, sediment erodability, and morphological changes on an intertidal mudflat. *Mar. Ecol. Progr. Ser.* **362**, 45–57.
- WOOD, C. J. 1967 Visualization of an incompressible wake with base bleed. *J. Fluid Mech.* **29**, 259–272 Part 2.
- ZONG, L. & NEPF, H. 2011 Spatial distribution of deposition within a patch of vegetation. *Water Resour. Res.* **47**, W03516.